



# Quantitative Evaluation of Supported Catalysts Key Properties from Electron Tomography Studies: Assessing Accuracy Using Material-Realistic 3D-Models

A. Bouzaine<sup>1</sup> · J. M. Muñoz-Ocaña<sup>2</sup> · A. Rodríguez-Chia<sup>2</sup> · A. B. Hungría<sup>1</sup> · J. J. Calvino<sup>1</sup> · M. López-Haro<sup>1</sup>

Accepted: 17 May 2022  
© The Author(s) 2022

## Abstract

Electron Tomography (ET) reconstructions can be analysed, via segmentation techniques, to obtain quantitative, 3D-information about individual nanoparticles in supported catalysts. This includes values of parameters out of reach for any other technique, like their volume and surface, which are required to determine the dispersion of the supported particle system or the specific surface area of the support; two figures that play a major role in the performance of this type of catalysts.

However, both the experimental conditions during the acquisition of the tilt series and the limited fidelity of the reconstruction and segmentation algorithms, restrict the quality of the ET results and introduce an undefined amount of error both in the qualitative features of the reconstructions and in all the quantitative parameters measured from them.

Here, a method based on the use of well-defined 3D geometrical models (phantoms), with morphological features closely resembling those observed in experimental images of an Au/CeO<sub>2</sub> catalyst, has been devised to provide a precise estimation of the accuracy of the reconstructions. Using this approach, the influence of noise and the number of projections on the errors of reconstructions obtained using a Total Variation Minimization in 3D (TVM-3D) algorithm have been determined. Likewise, the benefits of using smart denoising techniques based on Undecimated Wavelet Transforms (UWT) have been also evaluated.

The results clearly reveal a large impact of usual noise levels on both the quality of the reconstructions and nanometrological measurement errors. Quantitative clues about the key role of UWT to largely compensate them are also provided.

**Keywords** Supported catalysts · Electron Tomography · Nanometrology · Error assessment

## 1 Introduction

The potential of Electron Tomography to unveil the 3D structure of catalysts, with spatial resolution in the sub-nanometer scale, has been widely explored and reviewed in recent works [1, 2]. A variety of experimental techniques, based either on Transmission Electron Microscopy (TEM)

or Scanning Transmission Electron Microscopy (STEM) have been used to reveal different features of nanostructured catalysts in 3D, but High Angle Annular Dark Field imaging in STEM mode (HAADF-STEM) stands out as the most frequently used, given its chemical sensitivity and avoidance of imaging artifacts related to diffraction phenomena when dealing with crystalline materials[3].

Recently, the interest in the use of this characterization technique has moved from the determination of purely qualitative aspects to the quantification of structural parameters which determine materials performance, i.e. to *nanometrology*. In the case of catalysts, parameters like those related to exposed surfaces (specific surface area), pore structure (pore volume, outer/inner pore volume ratio or pore system connectivity and tortuosity), particle size distributions (average particle size and dispersion) or particle

✉ M. López-Haro  
miguel.lopezharo@uca.es

<sup>1</sup> Departamento de Ciencia de los Materiales e Ingeniería Metalúrgica y Química Inorgánica, Facultad de Ciencias, Universidad de Cádiz, Campus Río San Pedro, Puerto Real, 11510 Cádiz, Spain

<sup>2</sup> Departamento de Estadística e Investigación Operativa, Facultad de Ciencias, Universidad de Cádiz, Campus Río San Pedro, Puerto Real, 11510 Cádiz, Spain

morphology (e.g. measured as sphericity) are among those of major relevance[4–10].

Such quantification requires, as a previous step, splitting the whole reconstructed volume into background and object of interest. In many cases, the later has also to be separated into smaller components (objects) (e.g. supported particles and support or matrix and pores). The process of separation and object recognition is called *segmentation* [11]. Once segmented, the different objects in the reconstruction can be individually analysed, using different procedures, to measure a diversity of features (size, area, volume, roundness, roughness, ...). Then, from a sufficiently large set of measurements, a statistical analysis can be performed, which may lead to distributions of the different properties. These, in turn, can be used to determine parameters representative of the material as a whole, like average particle size, dispersion of the supported phase, average pore length/area/volume, etc.... This information, obtained at the nanoscale, can be further compared with that obtained at macroscopic level, for validation.

As evidenced in [5], a fruitful agreement between nanoscopic and macroscopic data, imposes a number of requirements. First, the collection of a large set of ET experiments; processing all the images in the tilt series images to attenuate the influence of noise; the optimization of reconstructions based on robust algorithms (e.g. Total Variation Minimization in 3D) and the use of automated, advanced, segmentation procedures. To complete all these tasks in a reasonable timeframe, a fully automated pipeline going from the sample to the final results, is needed [12]. Figure 1 depicts a schedule of the different steps involved in the whole quantification process using ET experiments. Certainly, the quality of the final results is influenced by each of these steps,

but reconstruction and segmentation are those with major contribution.

The goodness of the reconstruction algorithms is normally evaluated by applying them to well-defined input signals, so-called *phantoms*, made up of a collection of objects with a precise morphology and image intensity. Then, a figure of merit which measure the total deviation of the reconstructed pixel values from those in the model provide an estimation of the reconstruction error. Most frequently phantoms are 2D images. To date, algorithms based on Total Variation Minimization (TVM) have proved, in general, as the most accurate ones. These have demonstrated to suffer a smaller influence of noise; to minimise reconstruction artifacts due to incomplete sampling of the frequency space, i.e. the so-called missing wedge effect; and to be less sensitive to the reduction of the total number of projections in the tilt series[13, 14].

Segmentation involves partitioning the intensity histogram of the whole reconstructed volume into non-overlapping regions, which can then be individually assigned, by thresholding, to different components (void and objects). To improve this primary step in the metrological process, several works have proposed replacing conventional two-level thresholding, which works properly only for a very limited number of cases, by Otsu type [15, 16] thresholding or by more sophisticated approaches, as it is the case of anisotropic, nonlinear, diffusion (AND) [17]. Nevertheless, these global thresholding approaches fail in complex situations as are those frequently encountered with images of nanocatalysts. For these, customized methods [18] or the use of advanced clustering techniques [19] are required.

Independently from the particular reconstruction or segmentation procedures used in the 3D analysis of catalysts,

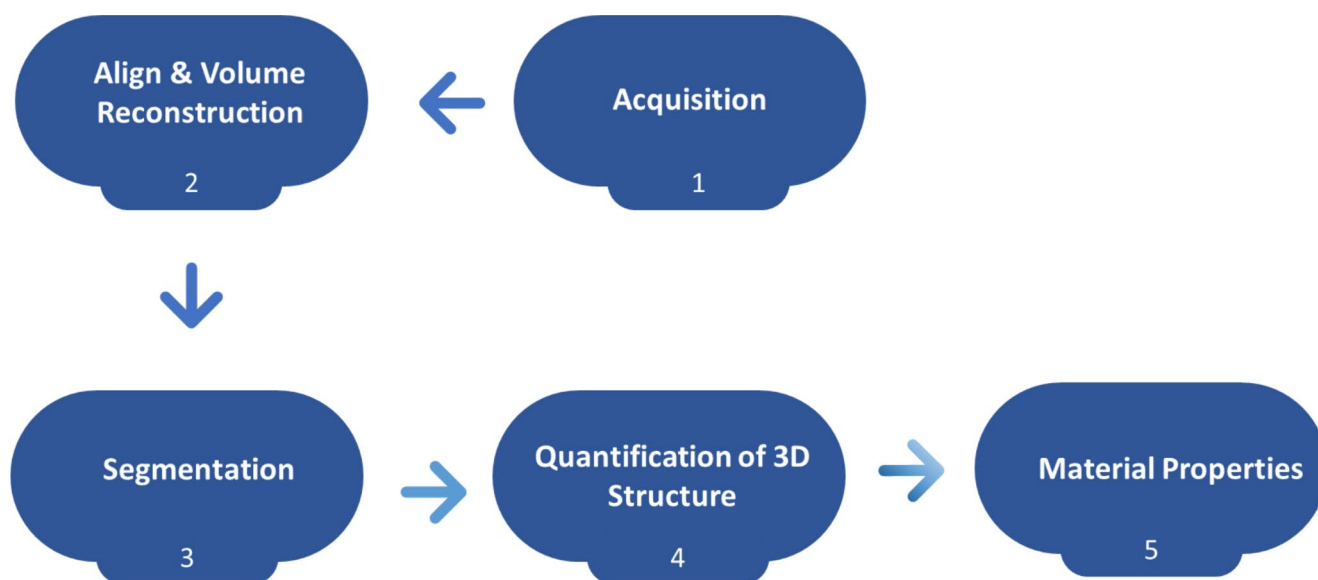


**Fig. 1** Scheme depicting the steps involved in Quantitative Analysis by Electron Tomography

an important issue which has not been properly addressed yet refers to the determination of the error of the quantifications made by ET. Given the complexity of the overall process, answering to this fundamental question is not a simple task. In fact, data resulting from the quantification of ET experiments routinely do not include estimates of error.

Recently, Wang et al. have studied the combined influence of reconstruction and segmentation fidelity in the analysis of the pore structure of a mesoporous carbon [20]. To this end, they used a 3D phantom with structural features close to those in the catalyst under analysis, to which they referred as a *material-realistic phantom*. To guarantee a close proximity between the model and the material under study, they employed as phantom a first reconstruction of an experimental tilt series obtained by DART (Discrete Algebraic Reconstruction Technique); a method which incorporates the segmentation step during reconstruction [21].

Although valid, this approach is limited, since it does not allow to incorporate in the phantom other features than those that can be actually retrieved by the reconstruction method employed. It will not provide information about details which are originally present in the material but get lost during the recovery of the 3D information. Moreover, a more in-depth analysis of the whole set of parameters which influence the quantification, requires taking into account other factors, which were not considered in this work, like noise or the total number of projections in the tilt series. The latter are two important parameters, particularly in the 3D analysis of beam sensitive materials, for which the use of a low dose of electrons, either by image or tilt under-sampling [22], is mandatory. It is clear that noise will involve errors in quantitative ET but quantifying their magnitude on each structural parameter and, more important, evaluating also in quantitative terms the impact of image denoising techniques are both questions of major practical importance. To highlight at this respect, Undecimated Wavelet Transform (UWT) has proven as a very powerful tool to dump noise effects on ET reconstructions [5, 23].

To overcome these limitations, here we propose the use as phantoms of geometrical 3D models with perfectly defined morphological features, which include objects and spatial relationships between these objects very close to those observed in experimental 2D HAADF-STEM images of the sample under study. The relative intensity of the different objects in the projections of the models should also match the values observed in the experimental 2D recordings.

To illustrate the potential of this approach, the analysis of 3D ET studies of a gold catalyst supported on CeO<sub>2</sub> is performed, focusing on the estimation of errors involved in the quantification of parameters like metallic nanoparticle dimensions (as a function of size and location on the support), roundness (morphology) or dispersion. Likewise,

errors associated to support parameters, like surface roughness or specific surface area, are also considered. In all cases, UWT, TVM-3D and the advanced segmentation method developed in [5] are used as tools to denoise the original tilt series, to reconstruct those series and to separate particle and support components, respectively.

Importantly, it will be also demonstrated that the a-priori knowledge obtained from the comparative analysis of the whole set of results obtained in our study provides relevant information to optimise the planification of experimental studies, this representing an actual synergy between theory and practice.

## 2 Experimental

The catalysts prepared for this study were synthesized employing a two-step preparation process. The ceria oxide nanocubes, CeO<sub>2</sub>-NC, were obtained by a hydrothermal method previously reported elsewhere [24]. The Au/CeO<sub>2</sub> catalyst was prepared via a deposition–precipitation procedure using HAuCl<sub>4</sub>·3H<sub>2</sub>O (99.99%, Alfa Aesar, 6.4 × 10<sup>-3</sup> M) as the gold precursor, Na<sub>2</sub>CO<sub>3</sub> (0.05 M) was used as precipitating agent and 5–7 g of support was employed in each synthesis. The gold precursor was added to the support in solution at pH 8 and at 60 °C for 1 h, under stirring and in absence of light. Afterward, the suspension was aged at the same conditions for 1 h. The obtained precipitate was filtered and washed with deionized water several times, and then dried at 100 °C overnight and pretreated in oxidant atmosphere at 500 °C. Details of the preparation procedure were similar to that followed by Daly et al. [25].

Gold loading was determined by ICP-AES and FRX. ICP measurement was carried out using ICP-AES Iris Intrepid equipment of Thermal Elemental. FRX was performed using a Bruker PIONEER 4 Kwatt power.

Specific surface area was determined using Micromeritics ASAP2020. Before the analysis, the sample was degassed for 2 h at 200 °C. Adsorption and desorption of nitrogen measurements were performed at -196 °C. Measurement of specific surface area was performed by multipoint on basis of the BET (Brunauer–Emmet–Teller) theory and equation.

Electron Tomography experiments were performed in a FEI Titan<sup>3</sup> Themis 60–300 Double Aberration Corrected microscope operated at 200 kV. A convergence angle of 9 mrad was selected in order to improve the depth of focus and a camera length of 115 mm was used, providing a 41–198 mrad collection angle. Tomography series were recorded within the -70° to +70° tilt range, acquiring a STEM-HAADF image every 2°, at a magnification of 450 K (0.18 nm pixel size) and using a dwell time of 10 ms.

The 3D material-realistic phantoms were built using the parametric equation of a sphere and a cube, and home-made Matlab scripts. The projections of the models were obtained using a routine from the ASTRA tomography toolbox (<http://www.astra-toolbox.com/index.html>). To this end, tilting around a single axis scheme was assumed for all the models. To add noise to the projections, routines implemented in MATLAB were used.

UWT denoising of the tilt series calculated from the phantoms, was performed using home-made scripts in MATLAB based on the WAVELAB850 toolbox ([http://statweb.stanford.edu/~wavelab/Wavelab\\_850/index\\_wavelab850.html](http://statweb.stanford.edu/~wavelab/Wavelab_850/index_wavelab850.html)) and the invansc packages, as downloaded from <http://www.cs.tut.fi/~foi/invansc/>. The whole set of HAADF-STEM denoised images were aligned combining cross-correlation methods, using FEI Inspect3D v 4.0 and the landmark-based alignment implemented in TomoJ [26]. The tilt series images were resized to  $512 \times 512$  px size, also background subtracted and normalized.

Compressed-Sensing Total Variation Minimization Algorithms (CS-TVM) were employed for the reconstruction, but following the optimization approach developed in [12] to ensure the best possible reconstruction within a

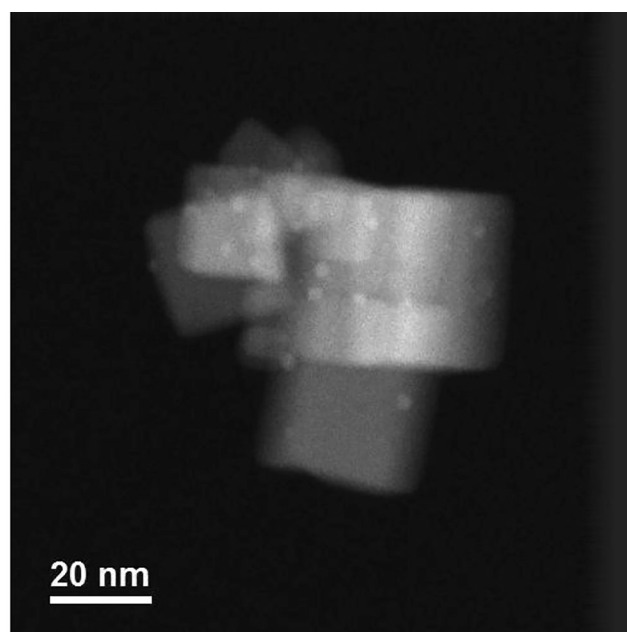


**Fig. 2** A representative STEM-HAADF image of the 0.8% Au/CeO<sub>2</sub>-NC catalyst

very wide range of reconstruction parameters. In particular,

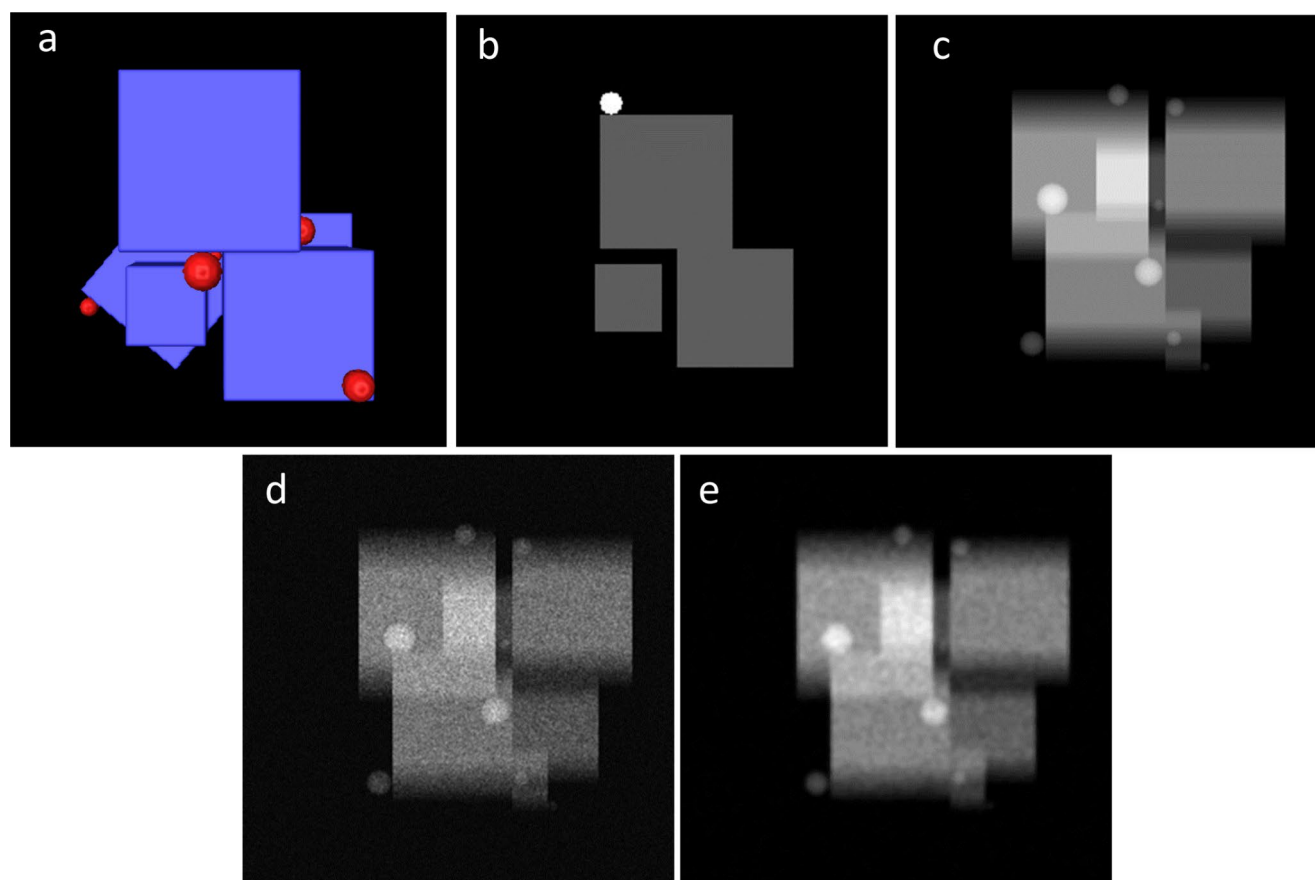


**Fig. 3** (a) 3D phantom; (b) a slice of the phantom to illustrate the relative intensities of supported phase and support; (c) projected phantom after tilting 5°; (d) noised phantom by adding a mixture of Poisson and Gaussian noise; (e) UWT-denoised phantom

for the optimization of CS-TVM, the denoised, filtered, and background subtracted images were reconstructed using the TVAL3 routine implemented in the ASTRA tomography toolbox. Once the reconstruction parameters were optimized, a final reconstruction of the tilt series was carried out using a TVM-3D algorithm implemented in Matlab. The segmentation step was carried out using a home-developed procedure [5]. For visualization and further nanometrological analysis of the reconstructed volumes, the FEI Avizo 7.0 Fire Software was used.

All the calculations were performed on an Intel Core I7 8700 workstation, equipped with 64 Gb RAM and VGA NVIDIA RTX 2070.

### 3 Results

The essential aspects of the methodology we propose are illustrated in the following through the quantitative analysis of ET experiments recorded on a supported metal catalyst. The features observed in 2D HAADF-STEM images of a

0.8% wt. Au/CeO<sub>2</sub> system, like that in Fig. 2 were used as reference to build the starting models.

#### 3.1 Phantom construction

Note that the catalyst is made up of cubed shaped ceria crystallites, in the 20–50 nm size range, which are in general not isolated but, instead, aggregated into medium-sized bunches. The cubes are partially contacting each other along their facets, keeping some of them in parallel orientation. The much smaller, rounded, objects correspond to Au nanoparticles, which range in size from 1 to 5 nm. Most of these particles sit on locations either close to the edges or in the boundary between neighbouring crystallites. Such a peculiar distribution of supported gold nanoparticles has been previously reported, from the qualitative analysis of ET experiments, for different Au catalysts supported on ceria-based oxides [27].

Taking into account these details, the *material-realistic* geometrical 3D model (phantom) shown in Fig. 3(a) was built. This phantom, which includes a total of 6 cubes of different size, simulates a bunch of contacting,

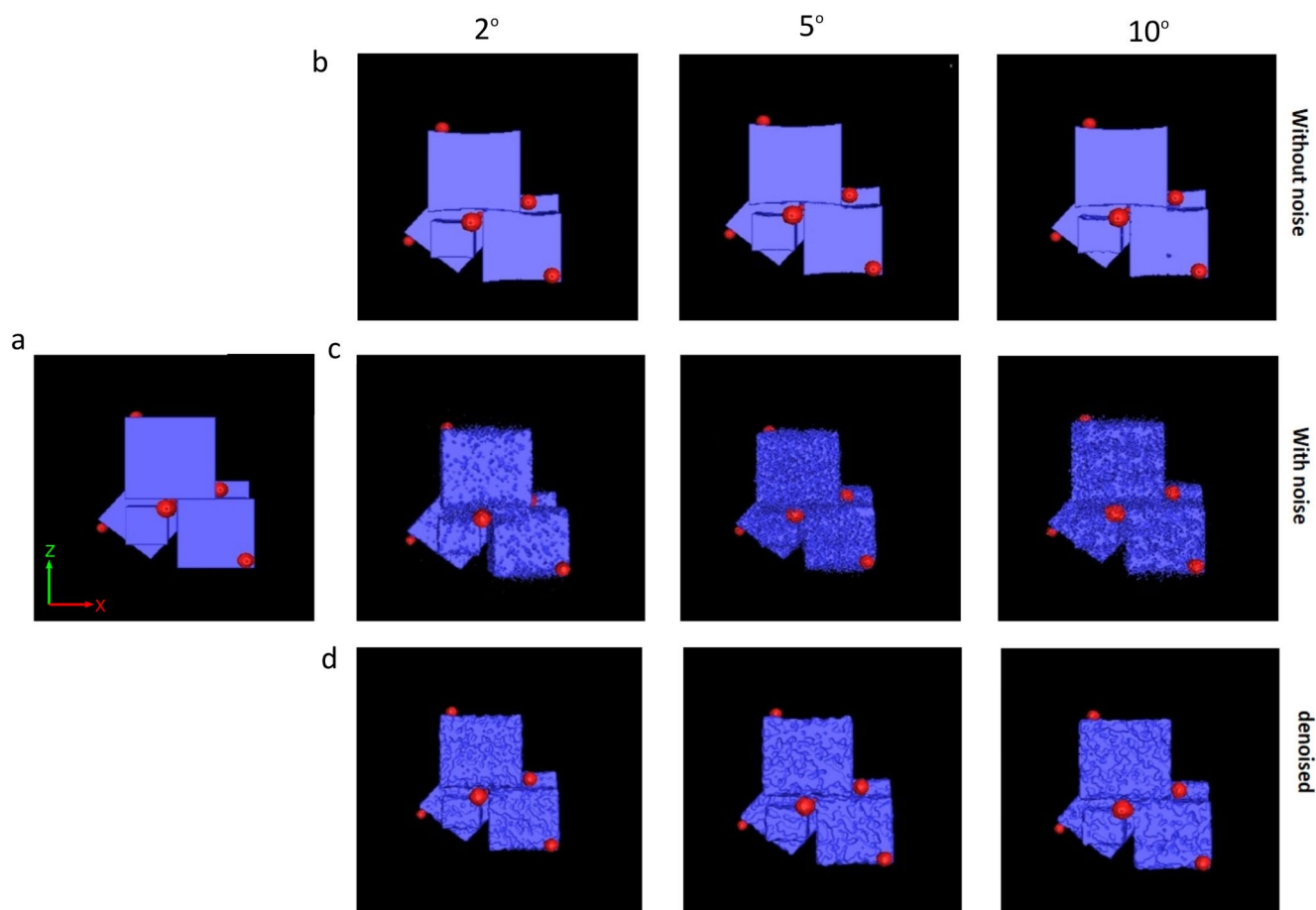


**Fig. 4** Rendering of: (a) model phantom; (1st row) reconstructions of phantom *a* obtained in the absence of noise; (2nd row) reconstructions after adding noise; (3rd row) reconstructions after UWT-denoising

parallel-oriented, crystallites. A total of 8 spherical particles of increasing diameters have been distributed on the surface of the cubes, in locations which resemble those in the experimental images, i.e. close to edges and at intercrystallite sites.

Apart from the dimensional details, a quite important question to fix in the phantom refers to the values of the voxels (i.e. the 3D counterparts of pixels) of particles and support, so that they reproduce the relative intensities observed in the experimental HAADF-STEM images. If we take into account that at low-medium magnification the intensity of these images scale with the product of density and thickness (i.e.  $I_{HAADF} \propto \rho t$ ) [28] and the densities of ceria (7.22 g/cm<sup>3</sup>) and gold (19.3 g/cm<sup>3</sup>), the  $I_{Au}/I_{CeO_2}$  ratio should be 2.7. The slice through the volume of the model shown in Fig. 3(b) illustrates the assignment of relative intensities for Au and CeO<sub>2</sub>. Note, in fact, that the voxels of the Au particles are much more intense than those of the support.

Figure 3(c) shows the projection of the model along the direction of the incoming beam of electrons in the absence of noise. As expected, the intensity of the particles which, in the observation direction, project outside the support boundaries appear with intensities similar or even lower than those of the support, due to the large difference in thickness of the two components. Those particles which project onto the support background appear much brighter, due to the superposition of the two components. Something similar occurs at the sites where different cubes overlap in projection.

To approach the characteristics of the experimental images, a mixture of Gaussian and Poisson noise was added to the model. Figure 3(d) shows the projection of the model after noise addition. The noised model was finally treated using UWT, Fig. 3(e). Note how this denoising technique retains the shape of the objects, avoiding artifacts at the boundaries, a question of major concern when recovering the morphology. Comparing the results obtained before and after denoising, the impact of noise on reconstruction errors can be evaluated.

### 3.2 Phantom reconstruction, segmentation and quantification

Figure 4 shows 3D volume renderings of the reconstructions of the phantom. To evaluate the influence of the total number of images in the tilt series, the reconstructions were made for tilt series considering projections in the  $-70^\circ$  -  $+70^\circ$  every  $2^\circ$  (left column),  $5^\circ$  (middle column) and  $10^\circ$  (right column). Likewise, three experimental conditions were considered, a tilt series made up of images with no noise (1st row), noisy images (2nd row) and UWT-denoised images (3rd row).

Concerning the reconstruction corresponding to the series where no noise was added, the following major ideas, related with qualitative comparisons between the different series and the phantom, are worth being mentioned: (1) with independence of size, all the facets of the cubes which are affected by the missing wedge effect (in this case those perpendicular to the x-axis) are reconstructed as concave surfaces, instead of flat. Moreover, curvature is not significantly affected by the number of images in the tilt series. On the contrary, those facets which are perpendicular or inclined with respect to the tilt axis (y-axis) are reconstructed as perfectly flat; (2) all the metal nanoparticles were detected in the reconstruction, even the smallest ones. The flat rounded morphology is also maintained.

When noise is present in the images of the tilt series, the reconstructions lead to rough cube surfaces, roughness increasing with decreasing the number of images in the tilt series. Roughening also affects the metal nanoparticles, whose size and shape is significantly modified in the reconstruction. As expected, the heterogeneity (not so sharp surfaces) induced by noise, gives rise to an attenuation of the curvature effect described in the previous paragraph.

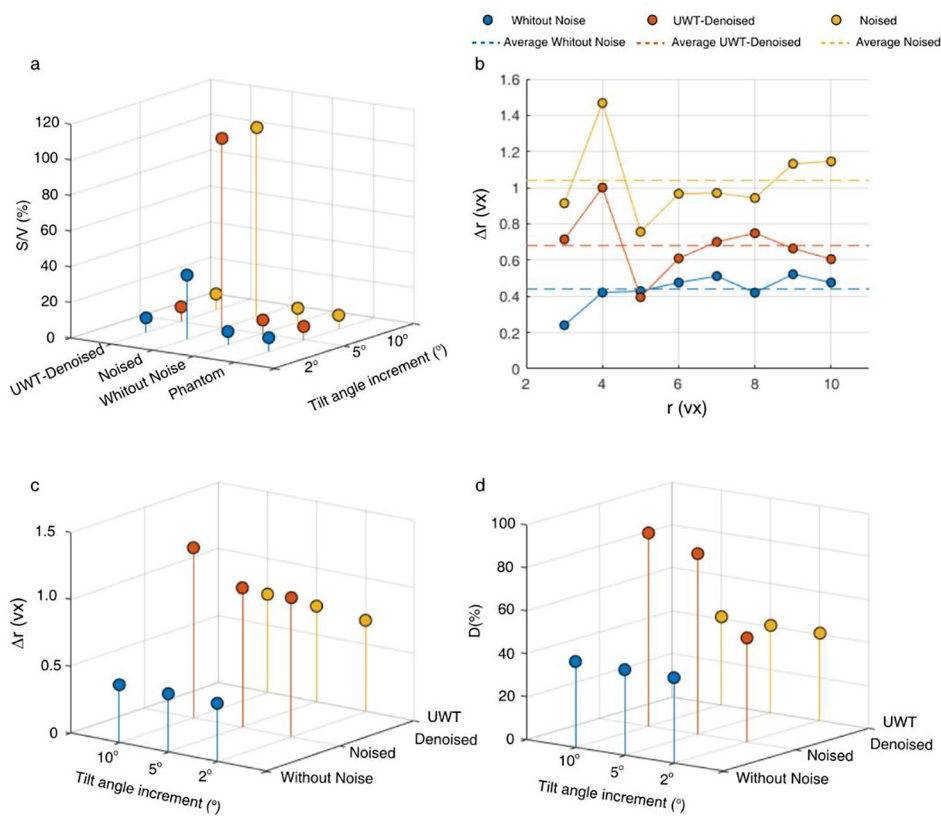
Finally, the mere visual inspection of the UWT-denoised series clearly reveals a large attenuation of the noised-induced roughening of the two components of the catalysts. Also important, shape and size of the metal nanoparticles is much better retained, as it will be better shown below on the grounds of quantitative arguments.

Concentrating now on quantitative aspects, Table S1 gathers the values of size, area and volume of the different ceria crystallites and gold nanoparticles involved in the phantom of Fig. 3(a). All the reconstructions gathered in Fig. 5 were segmented (Figure SI.1 illustrates the efficiency of the segmentation routine used here) and the following features measured: (1) volume, surface and equivalent diameter of each supported nanoparticles; (2) total volume and total surface of the support crystallites, Table S2. From these figures, interesting comparisons can be established with the reference values corresponding to the model.

We can start commenting on the values of the surface/volume ratio of the support crystallites as a whole, i.e. considering the 6 nanocubes; a basic parameter which is related to the specific surface area of this component of the catalyst. According to the bar graphs shown in Fig. 5(a), the values obtained when noise is not present are very close to those in the phantom, 7.7%. Moreover, the result is not sensitive to the number of images included in the tilt series.

Once noise is present in the tilt series, the difference with the phantom increases significantly and becomes extremely sensitive to the number of projections. Thus, the S/V ratio determined from the reconstruction of the tilt series with images from  $-70^\circ$  to  $+70^\circ$  every  $2^\circ$  (35.9%) overestimates a

**Fig. 5** (a) Values of the S/V ratios of the whole system of support nanocubes calculated from the phantom; reconstructions of the tilt series in the absence of noise; in the presence of noise and after UWT-denoising. (b) Difference between particle radius determined from ET ( $r_{ET}$ ) and the actual radius in the phantom ( $r_{ph}$ ) as a function of particle size. All values in voxels (vx); (c) Influence of tilt angle increment on the average value of  $\Delta r$ ; (d) Values of Dispersion determined from the whole set of reconstructions



lot the exact value in the phantom (7.7%), but the deviation increases a lot more when the images are recorded every 5° or 10°, for which the estimation increases up to roughly 106%.

This large error is related to the increase of total surface induced by the roughness observed in these reconstructions, Fig. 4(d). As previously commented, UWT-denoising corrects very efficiently this effect, leading to S/V ratios, with independence of the tilt angle increment, very close to that of the phantom. In fact, results are roughly the same as those obtained when noise is totally absent.

Other key parameters to be determined in this type of catalysts are the size of the supported nanoparticles and their morphology. As morphological parameter, the sphericity ( $\epsilon = \frac{\pi^{\frac{1}{3}}(6V)^{\frac{2}{3}}}{S}$ ) is proposed. This is just the ratio between the surface of the sphere with equivalent diameter (numerator in the equation) and the actual surface of the particle (denominator). Therefore, the value of  $\epsilon$  for a perfect sphere equals 1. Values lower than this (in the 1–0 range) indicate deviations from a perfect sphere. For a reference, the  $\epsilon$  value for a hemisphere is 0.83[29].

Figure 5(b) plots the difference between the radii of the 8 nanoparticles included in the model and the radii determined after reconstruction and segmentation. The dotted lines in this figure indicate the values of the average deviations in

the three cases analysed in this work, i.e. in the absence of noise, when noise is present and after denoising using UWT.

Note that, in general, the radii determined from the reconstructions are slightly smaller than those in the models. The difference amounts, in average, between 0.44 voxels (model without noise) and 1.04 voxels (noisy model). The first value represents the intrinsic, unavoidable, error associated to reconstruction and segmentation, whereas the latter includes the additional influence of noise. It is clear, in any case, that UWT denoising allows dumping very effectively this last contribution, decreasing the average error in the determination of particle radii to a value below 1 voxel.

In the three cases, the deviation of the errors from the average values is not larger than  $\pm 0.1$  voxels in the whole size range, this indicating a very mild influence of particle size on absolute error in the size determination. Larger differences are only observed in two cases, the particles of roughly 4 and 5 voxel size. As it can be observed in the 3D renderings shown in Figure SI2, this is related to the particular localization of these two particular nanoparticles in the model, surrounded by different support crystallites. Therefore, localization seems a much more influencing factor than size. Of course, relative error decreases with size from roughly 25% down to 5%. Therefore, using the combination of UWT, TVM 3D and the customized segmentation

procedure developed in [5], 0.7 voxels is a very good estimate of the error in ET measurement of particle size (radius).

Regarding the influence of tilt angle increment, Fig. 5(c), the average error in size determination by ET appears quite insensitive in the reconstruction of both the tilt series where noise is not present and the one denoised by UWT. In the case of the noisy one, increasing from 2° to 5° does not make a significant change, but for 10° tilt angle increments, the error in the radius determination increases up to, roughly, 1.2 voxels. These results indicate that as long as a proper denoising of the tilt series is performed, the use of large tilt angle increments still allows to obtain reconstructions from which the size of the supported particles can be recovered with a high degree of accuracy.

With the volume and surface area data, the dispersion of the system of supported particles can be also evaluated for the whole set of experiments, as  $D = \frac{\sum_i S_i}{\sum_i V_i}$ , where the summations extend to the whole set of particles and  $S_i$  and  $V_i$  refer to the values of surface and volume of each particle, Fig. 5(d). The actual dispersion of the Au particles in the model amounts to 38%. Note that an intrinsic error of +2%, which is independent of the angular sampling rate, is estimated for the reconstruction and segmentation process. This is expected, since the estimated error of roughly half a voxel in radius underestimates the actual size of the particle in the whole size range.

The presence of noise in the image tilt series gives rise to a large error in the estimation of dispersion, particularly

when the number of images in the tilt series is small. Importantly, UWT-denoising dumps very effectively the contribution of noise and provides dispersion values which are only +3% larger than the actual value in the model. This represents a relative error of 8%.

A final question that can be analysed refers to the morphology of the nanoparticles. In this case, to quantify the effects of reconstruction and segmentation on the modification of this aspect, the sphericity ( $\epsilon$ ) was used. Figure 5 shows a radial plot of the values of this parameter determined for the 8 Au particles included in the phantom of Fig. 3(a) for 2° (Fig. 6(a)), 5° (Fig. 6(b)) and 10° (Fig. 6(c)). Of course, all the particles in the phantom have values of  $\epsilon = 1$ . The morphology of the particles reconstructed in the presence of noise largely deviates from that of spheres, as it can be clearly observed in the radial graph, the largest deviations correspond to the two largest particles. Effectively, a detailed inspection of this reconstruction reveals nanoparticles with rather rough surfaces. Prior denoising using UWT allows to overcome the influence of noise,  $\epsilon$  values very close to 1 being observed for the UWT-denoised reconstruction. Therefore, UWT appears necessary to recover accurately not only the dimensions of the nanoparticles but also their shape.

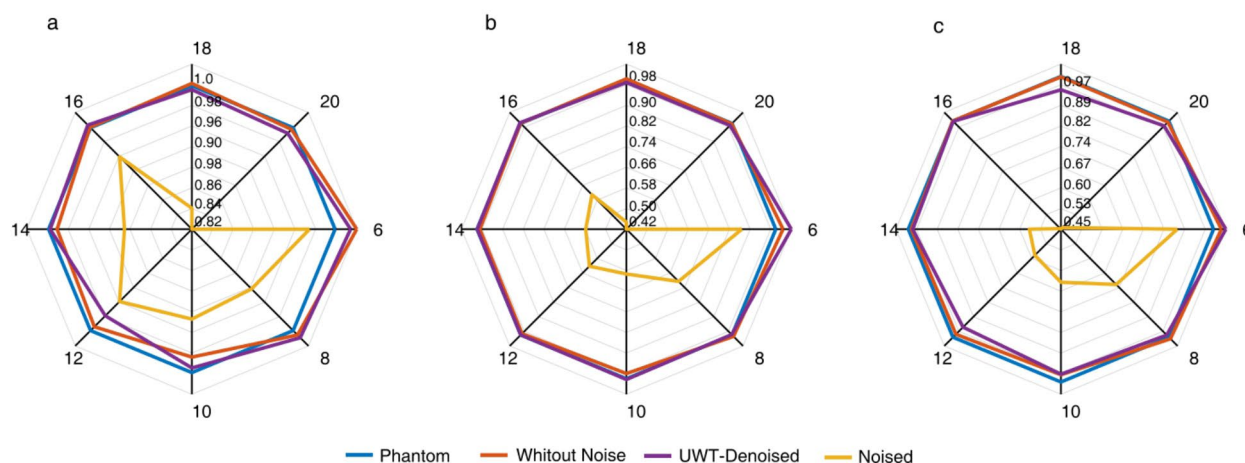
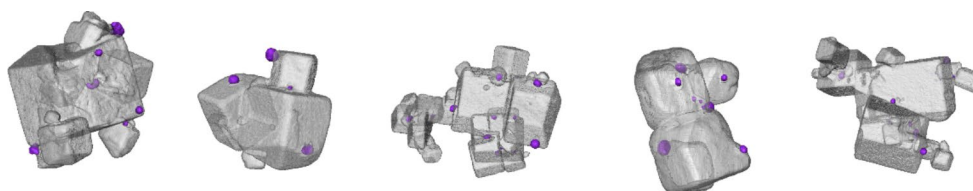


**Fig. 6** Sphericity of each of the 8 particles in the phantom of Fig. 3(a) for 2° (a), 5° (b) and 10° (c)

**Fig. 7** Volume rendering of TVM3D reconstructions obtained from tilt series at 5 different locations of an 0.8%wt Au/CeO<sub>2</sub>-NC catalyst





### 3.3 Study case: 0.8 wt% Au/CeO<sub>2</sub>-NC catalyst

This methodology was applied to the analysis of an ET study of a 0.8 wt Au/CeO<sub>2</sub>-NC which included 5 HAADF-STEM tilt series recorded in different locations of the catalyst. Figure 7 shows volume renderings of the TVM3D reconstructions after denoising all the images using UWT. The small volumes in blue correspond to the Au nanoparticles whereas the ceria support is displayed in light grey. Note that most CeO<sub>2</sub> crystallites are edge-and-corner-rounded cubes.

From these data, a number of catalyst parameters could be measured. Starting with the support, the specific surface area was determined to amount to 19.9 m<sup>2</sup>g<sup>-1</sup>. According to the results shown in the previous section, this parameter is expected to be overestimated by a 10% for reconstructions of UWT-denoised series acquired with tilt angle increments of 2° (see Fig. 5(a)). Therefore, a more accurate value for the surface area of this catalyst would be 18.1 m<sup>2</sup>g<sup>-1</sup>. The difference is rather small and any of the two values falls within the range estimated from N<sub>2</sub> physisorption isotherms of this catalyst, 19,0 ± 3,0 m<sup>2</sup>g<sup>-1</sup>, but the ET corrected figure is the most accurate this technique can provide.

Regarding the metallic phase, a first parameter which can be evaluated from the experimental series is their size, measured for example as equivalent diameter. Taking into account the results described in the previous section, these values should be increased by, roughly, 1.4 voxels (=2•0,68). Taking into account that the voxel size of the experimental tilt series was 0.18 nm/vox, this represents roughly 0.24 nm. Figure 8(a) shows the corresponding particle size distribution obtained from ET after incorporating this correction. The average diameter of the Au particles amounts to 4.4 nm, which is slightly larger than the value before correction, 4.0 nm. The reference figure which can be used for this parameter is the value determined from

2D HRTEM and HRSTEM images, which in this case was determined to amount to 4.7 nm.

Concerning the shape of the particles, Fig. 8(b) depicts the values of  $\epsilon$  for the whole set of particles as a function of their corrected size. To obtain this parameter, the corrections of both volume and area of each particle (as a function of size) were taken into account. Figure SI3(a), show the influence of particle size (in voxels) on the variation of the ratio between the surface segmented for each particle ( $S_{seg}$ ) and their actual surface in the phantom ( $S_{ph}$ ). Likewise, Figure SI3(b) shows the ratios corresponding to the volumes. Note that the deviations observed for small particles ( $r < 6$  voxels), both in surface and volume, are higher (average ratios around 0.56 and 0.43 for surface and volume respectively) than for the bigger ones ( $r > 9$  voxels), for which average ratios of 0.84 (surface) and 0.76 (volume) are found. Likewise, the deviations in volume are, for all sizes, bigger than deviations in surface. In the intermediate size region ( $5 < r < 9$  voxels), a linear relationship may be used for the correction of both surface and volume.

Considered as a whole, the system of particles presents an average sphericity of 0.90, whereas it amounts to 0.93 before corrections. Note, however, that most particles, 80%, have sphericity values in the 0.8–1.0 range, with an average of 0.94. Only a small fraction, 20%, of tiny ones (< 2 nm) are characterized by lower values, in the 0.6–0.7 range and average around 0.67. To understand the structural meaning of these figures, it is interesting to take into account the variation of  $\epsilon$  with the extent of truncation of a sphere along its diameter,  $\alpha$  ( $0 < \alpha < 2$ ). As shown in Figure SI4, with increasing  $\alpha$ ,  $\epsilon$  decreases from 1, the value expected for a perfect sphere, down to 0. For  $\epsilon=0.94$ , truncation takes place below the centre of the sphere,  $\alpha=0.55$ , giving rise to a particle with a contact angle with the surface,  $\theta$ , below 90° ( $\theta=63^\circ$ ).

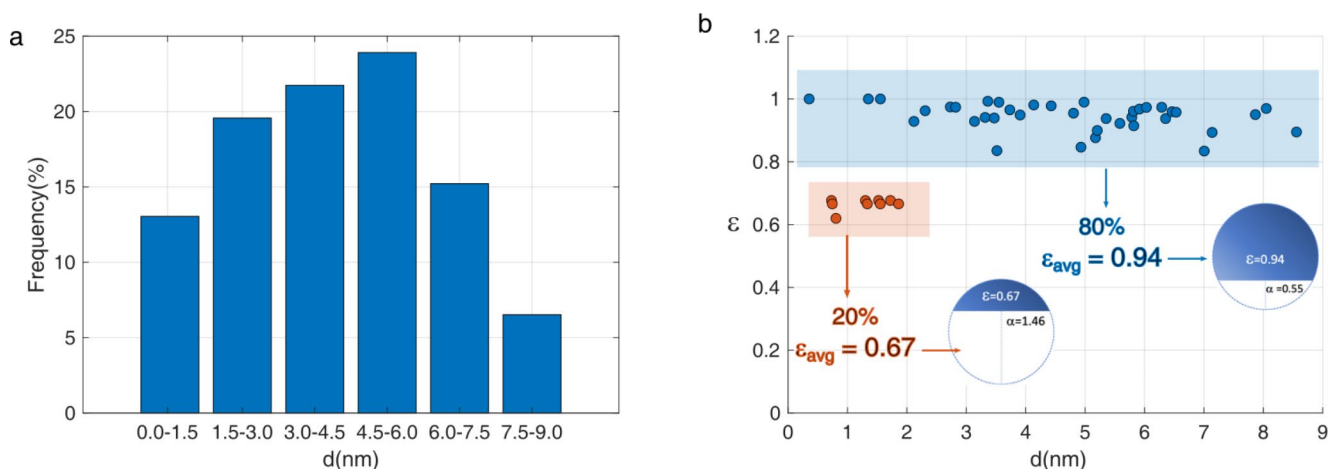


**Fig. 8** (a) Particle size distribution determined from the ET study, after correction of errors; (b) sphericity of metal particles as determined from ET, after volume and surface corrections, as a function of particle size

For  $\varepsilon=0.67$ , the sphere must be truncated at  $\alpha=1.46$ , this resulting in a flat particle, with  $\theta > 90^\circ$  ( $\theta=117^\circ$ ).

HRTEM and HRSTEM images have proven that Au nanoparticles grow epitaxially on the surface of ceria-based supports [30, 31], giving rise, in most cases, to two particle shapes; in fact, two types of truncated cube-octahedrons. A first one in which truncation leaves particles with contact angle lower than  $90^\circ$ , Figure SI4(c), and, in the case of smaller ones, particles in which the truncated cube-octahedron contacts the surface at angles greater than  $90^\circ$ , Figure SI4(b).

The presence of both type of particles is related to the balance between bulk and interface energies, which is a function of different parameters such as size, nature of the chemical gaseous environment surrounding the particle and exact structural nature of the Nanoarticle||Support interface. A study on a related Au/TiO<sub>2</sub> catalyst [32] suggests that the details of the metal||support interface, particularly the growth on the nanoparticles on faulted, stepped type, surfaces, largely influences the value of the H/W aspect ratio, at least for samples analysed under the UHV conditions characteristic of conventional HREM studies.

The lower spatial resolution of ET, in comparison with HRTEM or HRSTEM, and the inherently small size of the metal particles present in this type of catalysts (between 1 and 8 nm in diameter in the sample analysed here) allows to understand their detection as spherical-like objects in the ET experiments. In any case, it is clear that the methodology used here captures fine structural details of the morphology of the supported nanoparticles. This is possible due to the use of both a reconstruction algorithm, TVM3D, that avoids elongation artifacts and a segmentation method that does not disrupt the reconstructed morphology. The correction of surface and volume data is also important at this step.

With the set of corrected surfaces and volumes, a dispersion value for Au of  $D=0.18$  was estimated. This is just 0.1% below the value obtained before corrections, 0.19. The value determined from particle size distributions determined from 2D images, assuming a truncated cube-octahedron shape, amounts to 0.22. All these values are very close to each other, with differences between them within the experimental error of the macroscopic techniques used to determine this complex figure. As a reference, the value obtained by CO chemisorption at 35°C on the same catalyst was 0.22.

Since from ET, volume data about the two components of the system are available, another important parameter which can be evaluated for the whole catalyst is its metal loading. In this case both the correction of volumes of CeO<sub>2</sub> and Au have to be taken into account. By doing so, the value obtained in this case was 0.85% wt, again quite close to the value before correction 0.79% wt and within the range

determined from ICP and XRF,  $0.8 \pm 0.1\%$ wt. It is clear that this parameter of a supported catalysts will be determined by macroscopic techniques like the latter two, but the evaluation by ET is key since it provides a clue about the representativeness of the set of reconstructions collected for the sample. In other words, the agreement observed between macroscopic and ET evaluated parameters provide reliability to all the data which could be obtained from further analysis of the tilt series.

Summarising the results presented in this last section, using the quantitative data obtained in Sect. 3.2, it has been possible to correct the values of different structural parameters related to both the support and the supported phase. The corrections are in general of a small magnitude, which clearly points out to the adequacy of the whole procedure used to carry out the ET analysis, including the acquisition of the tilt series; their reconstruction using UWT denoised series and TVM3D algorithms and, finally, segmentation employing advanced routines. In any case, the values observed after correction are those that better represent the best results which can be obtained from the quantitative analysis of the reconstructed-segmented volumes of the catalyst. The good agreement between the corrected values of the different parameters and those obtained either by 2D Electron Microscopy or, more important, macroscopic techniques provide a high reliability to any structural feature which could be obtained from the reconstructed volumes.

## 4 Conclusions

A methodology to quantify the errors associated to the determination of different structural parameters of supported catalysts by Electron Tomography has been developed, which is based on the use of material-realistic 3D models with morphological and imaging characteristics close to those observed in 2D HAADF-STEM images.

This methodology allows to evaluate a-priori the influence of both experimental parameters and procedures involved in image reconstruction, like the tilt-angle increment or the use of denoising techniques. In the particular case analysed here, it becomes clear that UWT denoising is key to decrease errors. Moreover, the use of UWT-denoised series allows to increase the tilt-angle increment up to  $10^\circ$  without impacting on the reconstruction errors.

Regarding particle size, an error in the order of 1.4 voxels in the particle diameter, which is independent of particle size, is observed when the ET study is performed using TVM3D reconstructions and segmentation by advanced procedures. This represents relative errors in particle size ranging from roughly 20%, for the smallest particles, down to 5%, for the bigger ones. With these figures, it is possible

to determine the error expected for any particular particle size distribution determined from ET.

The methodology proposed allows also to quantify the error in the determination of dispersion. For the system of particles considered in our study, a value in the order of just 3% is observed. Likewise, the error in the analysis of morphological parameters, like sphericity can be also checked.

Although the particular case of a supported catalyst consisting of particles with well-defined shaped is considered, the approach would be valid for any other kind of nanostructured material, given the corresponding 3D models are built. In the most general case, a first approach to the most relevant morphological features can be obtained from an experimental reconstruction. Once these features have been identified (number and relative dimensions of the different components, their approx. morphology, presence of pores, aggregation state of the components or interactions between them,...) models in which all of them are perfectly controlled (in quantitative terms), and modified within a certain range, can be used to establish comparisons with those obtained for them from the quantification of their segmented 3D reconstructions. Only by doing so it is possible to establish the actual limits of our experimental approach and determine the magnitude of errors.

Finally, preliminary studies using this methodology allows not only to have an a-priori knowledge about the errors involved in the ET characterization of any type of material but also, very important, to establish the most appropriate experimental protocol to study it. This certainly represents a fruitful synergy between theory and experiments.

**Supplementary information** The online version contains supplementary material available at <https://doi.org/10.1007/s11244-022-01634-1>.

**Acknowledgements** This work has received support from Projects: PID2020-113006-RB-I00, PID2019-110018GA-I00, PID2020-114594GB-C22, funded by MCIN/AEI/ <https://doi.org/10.13039/501100011033>. This work has also been co-financed by Project ref: MAT2017-87579-R and by the 2014–2020 ERDF Operational Programme and by the Department of Economy, Knowledge, Business and University of the Regional Government of Andalusia, Project references: FEDER-UCA18-107139, FEDERUCA18-106895 and P18-FR-1422. STEM ET experiments were recorded at the DME-UCA Node of the Spanish Singular Infrastructure for Electron Microscopy of Materials (ICTS ELECMI).

**Funding** Open Access funding provided thanks to the CRUE-CSIC agreement with Springer Nature.

**Open Access** This article is licensed under a Creative Commons Attribution 4.0 International License, which permits use, sharing, adaptation, distribution and reproduction in any medium or format, as long as you give appropriate credit to the original author(s) and the source, provide a link to the Creative Commons licence, and indicate if changes were made. The images or other third party material in this

article are included in the article's Creative Commons licence, unless indicated otherwise in a credit line to the material. If material is not included in the article's Creative Commons licence and your intended use is not permitted by statutory regulation or exceeds the permitted use, you will need to obtain permission directly from the copyright holder. To view a copy of this licence, visit <http://creativecommons.org/licenses/by/4.0/>.

## References

- Hungria AB, Calvino JJ, Hernandez-Garrido JC (2019) HAADF-STEM Electron Tomography in Catalysis Research. *Top Catal* 62:808–821
- Midgley PA, Ward EPW, Hungria AB et al (2007) Nanotomography in the chemical, biological and materials sciences. *Chem Soc Rev* 36:1477–1494
- Su DS, Zhang B, Schlögl R (2015) Electron Microscopy of Solid Catalysts—Transforming from a Challenge to a Toolbox. *Chem Rev* 115:2818–2882
- Sakina F, Muñoz-Ocaña JM, Bouziane A et al (2019) Synthesis of mesoporous ceria using metal- and halogen-free ordered mesoporous carbon as a hard template. *Nanoscale Adv* 1:4772–4782
- Lopez-Haro M, Tinoco M, Fernandez-Garcia S et al (2018) A Macroscopically Relevant 3D-Metrology Approach for Nanocatalysis Research, Part. Part. Syst. Char., 35
- Grothausmann R, Zehl G, Manke I et al (2011) Quantitative Structural Assessment of Heterogeneous Catalysts by Electron Tomography. *J Am Chem Soc* 133:18161–18171
- Kübel C, Niemeier D, Cieslinski R et al (2010) Electron Tomography of Nanostructured Materials – Towards a Quantitative 3D Analysis with Nanometer Resolution, Materials Science Forum, 638–642, 2517–2522
- Friedrich H, Sietsma JRA, De Jongh PE et al (2007) Measuring Location, Size, Distribution, and Loading of NiO Crystallites in Individual SBA-15 Pores by Electron Tomography. *J Am Chem Soc* 129:10249
- Bals S, Batenburg KJ, Verbeeck J et al (2007) Quantitative three-dimensional reconstruction of catalyst particles for bamboo-like carbon nanotubes. *Nano Lett* 7:3669–3674
- Gommes CJ, de Jong K, Pirard J-P et al (2005) Assessment of the 3D Localization of Metallic Nanoparticles in Pd/SiO<sub>2</sub> Cogelled Catalysts by Electron Tomography, *Langmuir*, 21
- Gonzalez RC, Woods RE, Eddins SL (2009) *Digital Image Processing Using MATLAB*, 2nd Edition ed., Getesmark Publishing,
- Munoz-Ocana JM, Bouziane A, Sakina F et al (2020) Optimization of STEM-HAADF Electron Tomography Reconstructions by Parameter Selection in Compressed Sensing Total Variation Minimization-Based Algorithms, Part. Part. Syst. Char., 37
- Chen D, Goris B, Bleichrodt F et al (2014) The properties of SIRT, TVM, and DART for 3D imaging of tubular domains in nanocomposite thin-films and sections. *Ultramicroscopy* 147:137–148
- Goris B, Van den Broek W, Batenburg KJ et al (2012) Electron tomography based on a total variation minimization reconstruction technique. *Ultramicroscopy* 113:120–130
- Lopez-Haro M, Guétaz L, Printemps T et al (2014) Three-dimensional analysis of Nafion layers in fuel cell electrodes. *Nat Commun* 5:5229
- Hindson JC, Saghi Z, Hernandez-Garrido J-C et al (2011) Morphological Study of Nanoparticle – Polymer Solar Cells Using High-Angle Annular Dark-Field Electron Tomography. *Nano Lett* 11:904–909
- Fernández J-J, Li S (2003) An improved algorithm for anisotropic nonlinear diffusion for denoising cryo-tomograms. *J Struct Biol* 144:152–161

18. Leary R, Saghi Z, Armbrüster M et al (2012) Quantitative High-Angle Annular Dark-Field Scanning Transmission Electron Microscope (HAADF-STEM) Tomography and High-Resolution Electron Microscopy of Unsupported Intermetallic GaPd<sub>2</sub>Catalysts. *J Phys Chem C* 116:13343–13352
19. Liu L, Lopez-Haro M, Calvino JJ et al (2021) Tutorial: structural characterization of isolated metal atoms and subnanometric metal clusters in zeolites. *Nat Protoc* 16:1871–1906
20. Wang W, Svidrytski A, Wang D et al (2019) Quantifying Morphology and Diffusion Properties of Mesoporous Carbon From High-Fidelity 3D Reconstructions. *Microsc. Microanal* 25:891–902
21. Batenburg KJ, Bals S, Sijbers J et al (2009) 3D imaging of nanomaterials by discrete tomography. *Ultramicroscopy* 109:730–740
22. Vanrompay H, Béché A, Verbeeck J et al (2019) Experimental Evaluation of Undersampling Schemes for Electron Tomography of Nanoparticles. *Part. Part Syst Char* 36:1900096
23. Printemps T, Mula G, Sette D et al (2016) Self-adapting denoising, alignment and reconstruction in electron tomography in materials science. *Ultramicroscopy* 160:23–34
24. Mai H-X, Sun L-D, Zhang Y-W et al (2005) Shape-Selective Synthesis and Oxygen Storage Behavior of Ceria Nanopolyhedra, Nanorods, and Nanocubes. *J Phys Chem B* 109:24380–24385
25. Daly H, Goguet A, Hardacre C et al (2010) The effect of reaction conditions on the stability of Au/CeZrO<sub>4</sub> catalysts in the low-temperature water–gas shift reaction. *J Catal* 273:257–265
26. Messaoudi C, Boudier T, Sorzano COS et al (2007) TomoJ: tomography software for three-dimensional reconstruction in transmission electron microscopy. *BMC Bioinform* 8:288
27. Tinoco M, Fernandez-Garcia S, Lopez-Haro M et al (2015) Critical Influence of Nanofaceting on the Preparation and Performance of Supported Gold Catalysts. *ACS Catal* 5:3504–3513
28. Dutta A, Reid C, Heinrich H (2013) Simulation of Incoherent Scattering in High-Angle Annular Dark-Field Scanning Electron Microscopy. *Microsc Microanal* 19:852–853
29. Li T, Li S, Zhao J et al (2012) Sphericities of non-spherical objects. *Particuology* 10:97–104
30. López-Haro M, Yoshida K, del Río E et al (2016) Strain Field in Ultrasmall Gold Nanoparticles Supported on Cerium-Based Mixed Oxides, vol 32. Key Influence of the Support Redox State, *Langmuir*, pp 4313–4322
31. Akita T, Okumura M, Tanaka K et al (2005) TEM observation of gold nanoparticles deposited on cerium oxide. *J Mater Sci* 40:3101–3106
32. Gao W, Choi AS, Zuo J-M (2014) Interaction of nanometer-sized gold nanocrystals with rutile (110) surface steps revealed at atomic resolution. *Surf Sci* 625:16–22

**Publisher's note** Springer Nature remains neutral with regard to jurisdictional claims in published maps and institutional affiliations.